

Theoretical Study of One-Electron Oxidized Mn(III)– and Ni(II)–Salen Complexes: Localized vs Delocalized Ground and Excited States in Solution

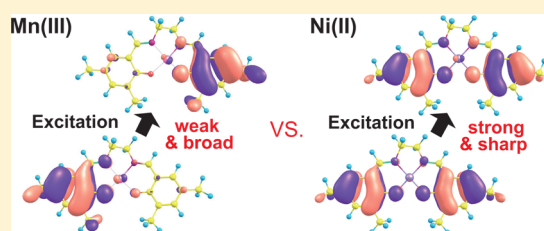
Shinji Aono,[†] Masayuki Nakagaki,[†] Takuya Kurahashi,[‡] Hiroshi Fujii,[‡] and Shigeyoshi Sakaki^{*,†}

[†]Fukui Institute for Fundamental ChemistryKyoto, University, Nishihiraki-cho, Takano, Sakyo-ku, Kyoto 606-8103, Japan

[‡]Institute for Molecular Science & Okazaki Institute for Integrative Bioscience, National Institutes of Natural Sciences, Myodaiji, Okazaki, Aichi 444-8787, Japan

S Supporting Information

ABSTRACT: One-electron oxidized Mn(III)– and Ni(II)–salen complexes exhibit unique mixed-valence electronic structures and charge transfer (CT) absorption spectra. We theoretically investigated them to elucidate the reason why the Mn(III)–salen complex takes a localized electronic structure (class II mixed valence compound by Robin–Day classification) and the Ni(II)–analogue has a delocalized one (class III) in solution, where solvation effect was taken into consideration either by the three-dimensional reference interaction site model self-consistent field (3D-RISM-SCF) method or by the mean-field (MF) QM/MM-MD simulation. The geometries of these complexes were optimized by the 3D-RISM-SCF-U-DFT/M06. The vertical excitation energy and the oscillator strength of the first excited state were evaluated by the general multiconfiguration reference quasi-degenerate perturbation theory (GMC-QDPT), including the solvation effect based on either 3D-RISM-SCF- or MF-QM/MM-MD-optimized solvent distribution. The computational results well agree with the experimentally observed absorption spectra and the experimentally proposed electronic structures. The one-electron oxidized Mn(III)–salen complex with a symmetrical salen ligand belongs to the class II, as experimentally reported, in which the excitation from the phenolate anion to the phenoxyl radical moiety occurs. In contrast, the one-electron oxidized Ni(II)–salen complex belongs to the class III, in which the excitation occurs from the doubly occupied delocalized π_1 orbital of the salen radical to the singly occupied delocalized π_2 orbital; the π_1 is a bonding combination of the HOMOs of two phenolate moieties and the π_2 is an antibonding combination. Solvation effect is indispensable for correctly describing the mixed-valence character, the geometrical distortion, and the intervalence CT absorption spectra of these complexes. The number of d electrons and the d orbital energy level play crucial roles to provide the localization/delocalization character of these complexes.



1. INTRODUCTION

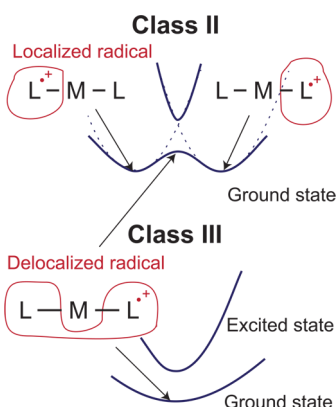
The mixed-valence complex has attracted much attention in both experimental and theoretical fields because it is potentially useful as a switching material and also a good model of electron transfer reaction, which is one of the most fundamental reactions in chemistry, physics, and biology.^{1–9} Generally, the mixed-valence complex contains more than two redox-active centers such as metal atoms and/or ligands that exhibit different formal oxidation states; for instance, Creutz–Taube ion is a typical mixed-valence complex which is the pyrazine-bridged Ru(II)–Ru(III) dimer.¹⁰ Central issues of the interests in the mixed-valence complex are how much electronic interaction is induced between two redox-active centers, how much it depends on metal, ligand, and solvent, and why. To understand the mixed-valence character, Robin and Day proposed three categories of mixed-valence compounds,¹¹ as shown in Scheme 1: (i) In the class I, the electronic interaction between two redox-active centers is too weak to cause the electron transfer. (ii) In the class II, the electronic interaction between two redox-active centers is enough for the electron

transfer reaction, but it is not so strong that each electronically localized state can be experimentally detected. (iii) In the class III, the electronic interaction between two redox-active centers is so strong that the delocalized state of an unpaired electron is experimentally observed. In general, the relative stabilities of the localized and the delocalized states of mixed-valence complexes are influenced very much not only by the direct interaction between neighboring moieties bearing mixed valence character but also by the interaction between the mixed valence moiety and the other environmental moiety. As a result, a number of complex systems exhibit an intermediate behavior between classes II and III.^{1–3} In particular, the solvation effect is crucial for determining the classification, because the localized state of the mixed-valence complex usually affords the considerably large dipole moment unlike the delocalized one, and hence, it is considerably stabilized by polar solvent.

Received: November 23, 2013

Published: February 11, 2014

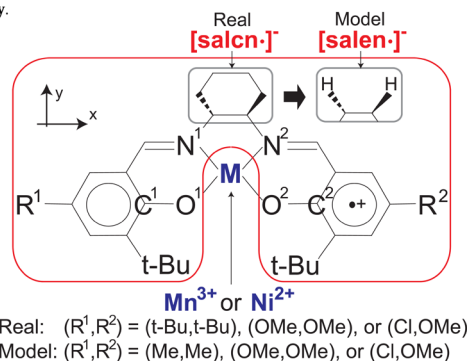
Scheme 1. Classification of Mixed-Valence Compounds and Potential Curves



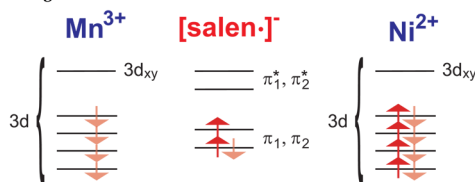
Recently, a unique mixed-valence compound, $[\text{Mn}^{\text{III}}(\text{salcn}^\bullet)]^{2+}$ **1_R** ($\text{H}_2\text{salcn} = N,N'$ -bis(3-tert-butyl-5R-salicylidene)-1,2-cyclohexanediamine), consisting of Mn(III) and one-electron oxidized salcn ligand was synthesized by Kurahashi and Fujii;¹² see Scheme 2 for its structure. Complex

Scheme 2. Structure of One-Electron Oxidized Metal–Salen Complex in Real and Model Systems

(a) Geometry.



(b) Electron configuration.



1_R takes a square planar structure, in which a phenoxyl radical is electronically linked to another distant phenolate through a redox-active Mn(III) center; in other words, the Mn(III) center bridges them with four coordination bonds. Interestingly, Kurahashi and Fujii provided an unambiguous assignment of the intervalence charge transfer (IVCT) band in **1_R** and discussed that the oxidation does not occur in the metal center but in the ligand. This is surprising because this observation suggests that the redox potential is not different so much between the Mn(III) and the phenolate in the salcn ligand; remember the previous report that the Mn(III)–phenoxyl radical species is readily converted to the Mn(IV)–phenolate species via the intramolecular electron transfer, which indicates that the Mn(III) is easier oxidized than the phenolate ligand.¹³ Interestingly, the IVCT band suggests that **1_R** belongs to the

class II mixed-valence compound with the localized electronic structure. This means that the IVCT band corresponds to the intramolecular electron transfer between two localized states, where one electron moves from the doubly occupied molecular orbital (DOMO) of one phenolate moiety to the singly occupied molecular orbital (SOMO) of another phenoxyl radical one. In contrast to **1_R**, the d^8 low-spin Ni(II) analogue, $[\text{Ni}^{\text{II}}(\text{salcn}^\bullet)]^+$ **2_R**, with the same one-electron oxidized salcn ligand belongs to the class III,^{12,14,15} where the delocalization of unpaired electron occurs between two redox-active centers in both the ground and the first excited states. These results indicate that the intramolecular electron transfer and the mixed-valence character largely depend on the metal species bridging two redox-active centers.

It is of considerable interest to theoretically elucidate the reason why **1_R** is classified into the class II but **2_R** is into the class III. It is still challenging for the theoretical study to provide the clear reason even nowadays, because these complexes have nearly degenerate electronic structure which is influenced very much by solvation effect. In other words, we must carry out multireference calculations of these transition metal complexes under consideration of solvation effect.

In the present work, we theoretically investigated the Mn(III)– and Ni(II)–salen complexes **1** and **2**, ($\text{H}_2\text{salen} = N,N'$ -bis(3-tert-butyl-5R-salicylidene)-1,2-ethylenediamine), which are models of **1_R** and **2_R**; see Scheme 2 and section 3. In the real system, bulky electron-donating tert-butyl (t-Bu) groups, less bulky electron-donating methoxy (OMe) groups, and electron-withdrawing Cl groups are introduced to the salen ligand, as shown in Scheme 2. Complexes **1** and **2** with Me, OMe, and Cl substituents were calculated here because their substituents significantly influence the energy level of the salen ligand and further the electronic structures of **1** and **2**.

To incorporate the solvation effect in the electronic structure calculation, we determined the geometry and the equilibrium solvation structure in the ground state by the 3D-RISM-SCF theory, because the 3D-RISM-SCF method has been successfully applied to large polar compounds such as transition metal complex and cellulose model compounds.¹⁶ In the RISM-SCF theory, the electronic structure of a solute molecule is solved by quantum mechanics in the presence of the effect of surrounding solvent molecules evaluated by classical statistical mechanics. The integral equation based on the statistical mechanics of liquid^{17,18} can provide an adequate ensemble of solvent configurations with less computational cost than the MD sampling like the QM/MM-MD method.^{19,20} Thereby, both solute electronic structure and equilibrium solvation structure can be simultaneously determined in a self-consistent manner. The 3D-RISM integral equation is based on the density functional theory of nonuniform polyatomic liquid proposed by Chandler et al.²¹ Later, Beglov and Roux applied the 3D hyper-netted chain (HNC) closure to the distribution of the monatomic Lennard–Jones (LJ) solvent²² and the 3D-RISM-HNC theory to the solvation of the polar molecules in H_2O solution.^{23,24} Kovalenko and Hirata derived the 3D generalization of the RISM method from the six-dimensional molecular Ornstein–Zernike integral equation by averaging out the rotational degrees of freedom of solvent.²⁵ Their method provides several merits compared to the PCM and the 1D-RISM-SCF methods, as follows: (i) The 3D-RISM theory improves a cavity formation effect, which is inherent in a bulky solute molecule such as glucosides and transition metal complexes. (ii) The 3D-RISM directly provides the information

about the solvation structure around the solute which considerably contributes to the stabilization and/or the destabilization via the solute–solvent electrostatic (ES) and the LJ interactions. (iii) To solve the 3D-RISM integral equation, we can use the ES potential (ESP) directly calculated by a solute electronic wave function unlike the 1D-RISM,²⁶ leading to the improvement of the accuracy and the convergence in the RISM-SCF cycle. However, it is still time-consuming to calculate the ESP with a solute wave function in the entire 3D grid space. To solve this difficulty without loss of accuracy, we recently constructed the three-regions 3D-RISM-SCF method¹⁶ by dividing the 3D grid space of solvent into the inner, outer, and switching regions, where the ESP of the inner region is directly evaluated with the solute electronic wave function, that of the outer region is approximately evaluated with the solute point charges, and they are smoothly connected in the switching region. This is a modification of the original method initially proposed by Yoshida and Hirata;²⁶ see refs 16 and 26 for details. We employed this method here.

The outline of this paper is as follows: In section 2, we explain the details of computational method to evaluate the vertical excitation energy and the oscillator strength in condensed phase using the general multiconfiguration reference quasi-degenerate perturbation theory (GMC-QDPT).^{27,28} In section 3, computational details are described. In section 4, we present the 3D-RISM-SCF-DFT-calculated geometry and localization/delocalization character of the salen ligand in the ground state and provide a comparison between GMC-QDPT calculations based on mean-field (MF) QM/MM-MD and 3D-RISM-SCF-calculated solvent distributions. Also, we discuss the difference in mixed-valence character between **1** and **2** and the important factors for determining the localization/delocalization character. The concluding remarks are summarized in section 5.

2. THEORETICAL METHOD

2.1. Vertical Excitation Energy and Oscillator Strength in Condensed Phase. In the condensed phase, the vertical excitation energy, ΔE_{cond} , at the given geometry, \mathbf{R} , of the solute and the given configuration, \mathbf{x} , of the solvent molecules is defined by the wave functions of the ground and the excited states $\bar{\Phi}_{\text{gr}}$ and $\bar{\Phi}_{\text{ex}}$, which are evaluated under the consideration of solvation, as follows:

$$\Delta E_{\text{cond}}(\mathbf{R}, \mathbf{x}) \equiv \Delta E_{\text{solu}}(\mathbf{R}, \mathbf{x}) + \Delta V_{\text{int}}(\mathbf{R}, \mathbf{x}) \quad (1)$$

where the first term is the change of the solute electronic energy by the excitation and the second term is that of the solute–solvent interaction energy by the excitation, as shown in eqs 2 and 3.

$$\Delta E_{\text{solu}} \equiv \langle \bar{\Phi}_{\text{ex}} | \hat{H}_{\text{gas}}(\mathbf{R}) | \bar{\Phi}_{\text{ex}}(\mathbf{R}, \mathbf{x}) \rangle - \langle \bar{\Phi}_{\text{gr}} | \hat{H}_{\text{gas}}(\mathbf{R}) | \bar{\Phi}_{\text{gr}}(\mathbf{R}, \mathbf{x}) \rangle \quad (2)$$

$$\Delta V_{\text{int}} \equiv \langle \bar{\Phi}_{\text{ex}} | \hat{V}_{\text{int}}(\mathbf{R}, \mathbf{x}) | \bar{\Phi}_{\text{ex}}(\mathbf{R}, \mathbf{x}) \rangle - \langle \bar{\Phi}_{\text{gr}} | \hat{V}_{\text{int}}(\mathbf{R}, \mathbf{x}) | \bar{\Phi}_{\text{gr}}(\mathbf{R}, \mathbf{x}) \rangle \quad (3)$$

where \hat{H}_{gas} is the electronic Hamiltonian in gas phase and \hat{V}_{int} is the solute–solvent interaction operator. This general definition of $\Delta E_{\text{cond}}(\mathbf{R}, \mathbf{x})$ is useful for the direct evaluation based on the usual QM/MM-MD simulation but not suitable for the evaluation by the present 3D-RISM method,¹⁶ because the 3D-RISM method does not employ the explicit positions of

solvent molecules but employs the statistical probability density functions at the 3D grid space of solvent, \mathbf{r} .

Here, we focus on the averaged absorption spectra, as shown in eq 4.

$$\Delta E_{\text{cond}}^{\text{avg}}(\mathbf{R}) \equiv \int d\mathbf{x} \Delta E_{\text{cond}}(\mathbf{R}, \mathbf{x}) P_{\text{gr}}(\mathbf{x}; \mathbf{R}) \approx \Delta E_{\text{solu}}^{\text{mf}} + \Delta V_{\text{int}}^{\text{mf}} \quad (4)$$

where P_{gr} is the probability density function with respect to the solvent configuration, \mathbf{x} , in the ground state. The first and the second terms of eq 4 are described as follows.

$$\Delta E_{\text{solu}}^{\text{mf}} \equiv \langle \bar{\Phi}_{\text{ex}}^{\text{mf}} | \hat{H}_{\text{gas}}(\mathbf{R}) | \bar{\Phi}_{\text{ex}}^{\text{mf}}(\mathbf{R}; g_{\text{gr}}) \rangle - \langle \bar{\Phi}_{\text{gr}}^{\text{mf}} | \hat{H}_{\text{gas}}(\mathbf{R}) | \bar{\Phi}_{\text{gr}}^{\text{mf}}(\mathbf{R}; g_{\text{gr}}) \rangle \quad (5)$$

$$\Delta V_{\text{int}}^{\text{mf}} \equiv \langle \bar{\Phi}_{\text{ex}}^{\text{mf}} | \hat{V}_{\text{int}}^{\text{mf}}(\mathbf{R}; g_{\text{gr}}) | \bar{\Phi}_{\text{ex}}^{\text{mf}}(\mathbf{R}; g_{\text{gr}}) \rangle - \langle \bar{\Phi}_{\text{gr}}^{\text{mf}} | \hat{V}_{\text{int}}^{\text{mf}}(\mathbf{R}; g_{\text{gr}}) | \bar{\Phi}_{\text{gr}}^{\text{mf}}(\mathbf{R}; g_{\text{gr}}) \rangle \quad (6)$$

The $g_{\text{gr}}(\mathbf{r})$ of eqs 5 and 6 is the equilibrium solvation structure around the solute in the ground state and the $\bar{\Phi}_{\text{gr}}^{\text{mf}}$ and $\bar{\Phi}_{\text{ex}}^{\text{mf}}$ are the solute wave functions corresponding to the ground and the excited states, respectively, which are the eigen-states of the mean-field (MF) Hamiltonian in the condensed phase, $\hat{H}_{\text{gas}}(\mathbf{R}) + \hat{V}_{\text{int}}^{\text{mf}}(\mathbf{R}; g_{\text{gr}})$.

The solute–solvent interaction term, $\hat{V}_{\text{int}}^{\text{mf}}(\mathbf{R}; g_{\text{gr}})$, in eq 4 is evaluated here by eqs 7 and 8;

$$\hat{V}_{\text{int}}^{\text{mf}}(\mathbf{R}; g_{\text{gr}}) = \rho \sum_s q_s \int d\mathbf{r} g_{\text{gr}s}(\mathbf{r}) \hat{V}_{\text{int}}^{\text{p}}(\mathbf{R}, \mathbf{r}) \quad (7)$$

$$\hat{V}_{\text{int}}^{\text{p}}(\mathbf{R}, \mathbf{r}) \equiv w(\mathbf{r}) \left\{ \sum_{i \in \text{electron}} \frac{-1}{|\mathbf{r}_i - \mathbf{r}|} + \sum_a \frac{Z_a}{|\mathbf{R}_a - \mathbf{r}|} \right\} + (1 - w(\mathbf{r})) \sum_a \frac{\hat{Q}_a}{|\mathbf{R}_a - \mathbf{r}|} \quad (8)$$

where the ρ is the number density of solvent molecules, the q_s is the partial charge of the solvent site s , the Z_a is the nuclear charge on the solute site a , \hat{Q}_a is the operator generating the effective point charge on the solute site a by the least-squares fitting,¹⁹ the $\hat{V}_{\text{int}}^{\text{p}}$ is the ES potential operator,²⁹ and the $w(\mathbf{r})$ is the switching function introduced to reduce the computational cost of the three-regions 3D-RISM-SCF calculation.¹⁶

In the MF approximation, the oscillator strength, $f_{\text{gr,ex}}^{\text{avg}}$, is also evaluated by the $\bar{\Phi}_{\text{gr}}^{\text{mf}}$ and $\bar{\Phi}_{\text{ex}}^{\text{mf}}$ in the similar manner to the $f_{\text{gr,ex}}^{\text{gas}}$ in gas phase,³⁰ as shown in eq 9.

$$f_{\text{gr,ex}}^{\text{avg}} \equiv \frac{2m_e}{3\hbar^2} \Delta E_{\text{cond}}^{\text{avg}} |\langle \bar{\Phi}_{\text{gr}}^{\text{mf}} | \sum_{i \in \text{electron}} \hat{\mathbf{r}}_i | \bar{\Phi}_{\text{ex}}^{\text{mf}}(\mathbf{R}; g_{\text{gr}}) \rangle|^2 \quad (9)$$

where the m_e is the mass of electron and the $\hat{\mathbf{r}}_i$ is the position operator of the i -th electron. The Condon approximation³¹ is employed in all these equations and the Franck–Condon factor is approximately taken to be 1.0 in eq 9.

2.2. GMC-QDPT Calculation in Condensed Phase. As mentioned above, the multireference computational method must be employed, because the mixed-valence complex has two states close to each other in energy at least. In the present study, we evaluated the $\bar{\Phi}_{\text{gr}}^{\text{mf}}$ and $\bar{\Phi}_{\text{ex}}^{\text{mf}}$ in eqs 4, 5, 6, and 9 at the GMC-QDPT level²⁷ with the given optimized geometry, \mathbf{R}^{opt} , and the given distribution function of the solvent, $g_{\text{gr}}(\mathbf{r})$. To this aim, the electronic Hamiltonian in gas phase, $\hat{H}_{\text{gas}}(\mathbf{R})$, must be replaced with that in the condensed phase, $\hat{H}_{\text{gas}}(\mathbf{R}) +$

$\hat{V}_{\text{int}}^{\text{mf}}(\mathbf{R}; g_{\text{gr}})$, and then, the effective Hamiltonian must be constructed with the GMC-QDPT method.

This can be straightforwardly performed with simple modification of original codes of GMC-QDPT by adding the following one-electron integral term to the Fock matrix in gas phase, $\mathcal{F}_{\mu\nu}^{\text{gas}}$,

$$\mathcal{F}_{\mu\nu}^{\text{solv}} = \mathcal{F}_{\mu\nu}^{\text{gas}} + \langle \chi_{\mu} | \hat{V}_{\text{int}}^{\text{mf}}(\mathbf{R}; g_{\text{gr}}) | \chi_{\nu}(\mathbf{R}) \rangle \quad (10)$$

where χ_{μ} and χ_{ν} represent the atomic orbitals. The similar modification was previously made in the RISM-CASSCF/MRMP2^{32,33} and the RISM-SA-CASSCF/MS-CASPT2 methods³⁴ by Kato and his co-workers.

This modification provides the energies of ground and excited states, $E_{\text{gr}}^{\text{cond}}$ and $E_{\text{ex}}^{\text{cond}}$, at the GMC-QDPT level, which consist of the solute electronic energy and the solute–solvent ES interaction energy in the condensed phase,

$$E_{\text{gr}}^{\text{cond}} \equiv \langle \bar{\Phi}_{\text{gr}}^{\text{mf}} | \hat{H}_{\text{gas}}(\mathbf{R}) + \hat{V}_{\text{int}}^{\text{mf}}(\mathbf{R}; g_{\text{gr}}) | \bar{\Phi}_{\text{gr}}^{\text{mf}}(\mathbf{R}; g_{\text{gr}}) \rangle \quad (11)$$

$$E_{\text{ex}}^{\text{cond}} \equiv \langle \bar{\Phi}_{\text{ex}}^{\text{mf}} | \hat{H}_{\text{gas}}(\mathbf{R}) + \hat{V}_{\text{int}}^{\text{mf}}(\mathbf{R}; g_{\text{gr}}) | \bar{\Phi}_{\text{ex}}^{\text{mf}}(\mathbf{R}; g_{\text{gr}}) \rangle \quad (12)$$

In summary, we can evaluate the $\Delta E_{\text{cond}}^{\text{avg}}$ as the difference between the $E_{\text{gr}}^{\text{cond}}$ and the $E_{\text{ex}}^{\text{cond}}$ and also the $\Delta V_{\text{int}}^{\text{mf}}$ as the product of the solute–solvent ES interaction matrix, $V_{\text{int}\mu\nu}^{\text{mf}}$, and the difference in density matrix between the ground and excited states, $\Delta D_{\mu\nu}^{\text{PT}}$, at the GMC-QDPT level.

3. COMPUTATIONAL DETAILS

To reduce the computational cost, we employed the salen ligand as a model of the salcn ligand in **1**_R and **2**_R as follows: (i) all t-Bu groups of the salcn ligand were replaced by methyl (Me) groups. This substitution is reasonable because the replacement of t-Bu group with Me group changes the distance little between two phenolate moieties; remember that the distance between two phenolate moieties becomes longer if the t-Bu induces the steric repulsion with each other. (ii) Cyclohexyl moiety (–C₆H₁₀–) of the salcn ligand was replaced by the C₂H₄ moiety with which the salcn is modified to the salen; see Scheme 2. Though this substitution leads to the loss of the chirality of the metal–salcn complex, the geometry of the remaining parts of the solute and its radical character of the ground and the first excited states are influenced only slightly by this simplification;³⁵ see Supporting Information Figure S1 for details.

To calculate the averaged vertical excitation energy $\Delta E_{\text{avg}}^{\text{cond}}$ and the oscillator strength $f_{\text{gr,ex}}^{\text{avg}}$ by eqs 4 and 9, respectively, the optimized geometry, \mathbf{R}^{opt} , of the solute and the solvent distribution function, $g_{\text{gr}}(\mathbf{r})$, must be determined in the ground state of the metal–salen complexes. To this aim, we applied the three-regions 3D-RISM-SCF method¹⁶ to the Mn(III)– and the Ni(II)–salen model complexes **1** and **2**, where three sets of (a) (Me, Me), (b) (OMe, OMe), and (c) (Cl, OMe) were employed for the substituents (R^1, R^2) on the salen ligand; see Supporting Information Figure S1. For convenience, the Mn(III) and Ni(II) complexes **1** and **2** with the substituents (R^1, R^2) = (Me, Me), (OMe, OMe), and (Cl, OMe) are named **1a**, **1b**, and **1c** and **2a**, **2b**, and **2c**, respectively, hereafter.

Prior to starting to describe the computational details, we wish to mention the electronic structures of **1** and **2** for better understanding; see Scheme 2b. According to the experimental report, both the Mn and the salen moieties have radical centers in **1**. In **2**, on the other hand, only the salen moiety has a radical

center but the Ni(II) has a closed shell d⁸ electron configuration.

The geometry optimization was performed by the 3D-RISM-SCF-U-DFT method with the M06 functional,³⁶ as will be explained in section 4.1; we focused on the doublet state in the Ni(II) complex **1** and the quartet state in the Mn(III) complex **2**, because the quartet state is more stable than the sextet state in the Mn(III) complex **1**; see Supporting Information Table S1. This is not surprising because the Mn(III) ion with a d⁴ electron configuration tends to take a high spin quintet state and therefore the quartet state is constituted with one α -electron on the salen ligand and four β -electrons on the Mn d orbitals, where unpaired electron of the salen ligand is defined to take α -spin for convenience hereafter.

To investigate the vertical excitation, we used the two-state average GMC-QDPT method for the ground and the first excited states, where we considered two parent determinants corresponding to the main configurations of the ground and the first excited states and then constructed the configuration interaction (CI) space by allowing single and double excitations from the two parent determinants to the excited determinants. To include the solvation effect, we used the 3D-RISM-SCF-U-DFT/M06-calculated solvent distribution function for $g_{\text{gr}}(\mathbf{r})$ in eq 10; we named this computational method “3D-RISM-GMC-QDPT” hereafter. For the Ni(II) complex **2**, 18 orbitals were chosen for the active space, which correspond to all the π orbitals of two pairs of *o*-cyano-phenolate moieties in the salen ligand.³⁷ For the Mn(III) complex **1**, four singly occupied 3d orbitals (d_{xz} , d_{yz} , d_z , and $d_{x^2-y^2}$) were further added to the active space.³⁷ The GMC-QDPT calculation with these small active spaces (SASs) is hereafter denoted by GMC-QDPT-(SAS/SAS). However, all the 3d orbitals of the metal center were not included in these SASs. In general, the d orbitals of the metal center play an important role in determining the electronic structure. Hence, it is necessary to investigate whether such active space is reasonable or not. After checking that the GMC-QDPT calculations with these SASs provide reasonable results, we added further 8 orbitals to the active space of **1** and 16 orbitals to that of **2** to include all 3d orbitals in a large active space (LAS) and performed the GMCSCF-(LAS) calculations; see Supporting Information pages S3–S4 for details of these LASs. Finally, we selected 25 orbitals for the medium active space (MAS) by removing 5 orbitals and 9 orbitals from the LASs of **1** and **2** to reconstruct the reference states, respectively, and performed the successive QDPT calculation of the vertical excitation energy $\Delta E_{\text{cond}}^{\text{avg}}$ and the oscillator strength $f_{\text{gr,ex}}^{\text{avg}}$.³⁸ For convenience, this method is named GMC-QDPT(LAS/MAS) hereafter, where the LAS before slash represents the active space for GMCSCF calculation and the MAS after slash is the active space for QDPT calculation. In the GMC-QDPT(LAS/MAS) calculation, the $\sigma \rightarrow d_{xy}$ excitation configuration is explicitly included in the CI space, and also, the $d_{\pi} \rightarrow \pi$ excitations are involved in the Ni(II) complex **2**.³⁸

In all the above calculations, the (31111/22111/411/1) basis sets were used for valence electrons of Mn and Ni atoms, where their 10 core electrons were replaced with the Stuttgart/Dresden (SDD) effective core potentials (ECPs).³⁹ For other atoms, cc-pVDZ basis sets were employed, where augmented functions were added to O, N, and Cl atoms.⁴⁰

When the solvation structure $g_{\text{gr}}(\mathbf{r})$ was determined by the 3D-RISM integral equation, we employed the Kovalenko–Hirata (KH) closure.²⁵ As the initial step of the 3D-RISM-SCF-

Table 1. Important Geometrical Parameters, α -Component of Dipole Moment μ_x , and Difference in Free Energy between C_1 - and C_2 -Symmetrical Geometries, $\Delta A(C_1-C_2)$, in One-Electron Oxidized Mn(III)–Salen Complexes

Mn(III) (R^1, R^2)	gas or solv.	sym.	L or D ^b	bond length ^a [Å]				μ_x^c	$\Delta A(C_1-C_2)^d$
				C–O ¹	C–O ²	M–O ¹	M–O ²		
R ¹ = R ² Case									
1a (Me,Me)	gas	C ₁	L ^b	1.32	1.27	1.80	1.90	6.1	−0.18
	CH ₂ Cl ₂	C ₁	L	1.32	1.27	1.80	1.91	9.1	−1.24
	H ₂ O	C ₁	L	1.32	1.27	1.82	1.92	11.6	−2.52
1b (OMe,OMe)	gas	C ₂ -like	D ^b	1.30	1.30	1.84	1.84	0.5	−0.03
	CH ₂ Cl ₂	C ₁	L	1.32	1.28	1.81	1.90	10.5	−0.97
	H ₂ O	C ₁	L	1.32	1.28	1.82	1.91	13.8	−2.55
R ¹ ≠ R ² Case									
1c (Cl,OMe)	gas	C ₁	L	1.32	1.28	1.80	1.90	12.8	
	CH ₂ Cl ₂	C ₁	L	1.32	1.28	1.81	1.90	15.7	
	H ₂ O	C ₁	L	1.32	1.28	1.82	1.89	18.2	

^aSee Scheme 2 for positions of O¹ and O² atoms. ^bL and D represent the localized and delocalized electronic states, respectively. ^cUnit is [Debye].^dUnit is [kcal mol^{–1}]

U-DFT calculation, the 1D-RISM calculation was carried out to set up the solvent–solvent total correlation functions with the density $\rho = 1.327 \text{ g cm}^{-3}$ and temperature $T = 203.0 \text{ K}$ for dichloromethane (CH₂Cl₂) solvent, which are the same as in the experiment.¹² As a reference for the strongly polar solvent, we also calculated with $\rho = 1.00 \text{ g cm}^{-3}$ and $T = 298.15 \text{ K}$ for H₂O solvent. The point charges and the LJ parameters of CH₂Cl₂ solvent were taken from the five sites model⁴¹ and those of water solvent were taken from the SPC model⁴² by modifying the LJ parameters of the Hw atom, $(\sigma_{\text{Hw}}, \epsilon_{\text{Hw}}) = (1.0 \text{ Å}, 0.056 \text{ kcal mol}^{-1})$,^{19,20} where the H and O sites of water solvent are hereafter denoted by Hw and Ow, respectively, for convenience. The 1D-RISM calculation was performed on a grid of 8096 points, corresponding to the 1D space radius of 56.2 Å. In the 3D-RISM calculation, the LJ parameters of solute molecules were taken from AMBER⁴³ except for Mn and Ni atoms. For Mn(III) and Ni(II), we determined the LJ parameters by fitting the M06 potential energy profile of metal–salen complexes with one CH₂Cl₂ molecule: They are $(\sigma_{\text{Mn}}, \epsilon_{\text{Mn}}) = (3.44 \text{ Å}, 0.297 \text{ kcal mol}^{-1})$ and $(\sigma_{\text{Ni}}, \epsilon_{\text{Ni}}) = (3.57 \text{ Å}, 0.144 \text{ kcal mol}^{-1})$. As a box size of solvent, we set a cubic grid of 256 points/axis with the spacing of 0.25 Å for the geometry optimization and the evaluation of the vertical excitation with the GMC-QDPT method. To divide the solvent grid space into three regions, the boundary distances of r_{in} and r_{out} are taken to be 15.0 and 18.0 Å, respectively; see ref 16 for the definition.

We implemented the present 3D-RISM-SCF method into the GAMESS program code.⁴⁴ For the purpose of comparison, the vertical excitation energy and the oscillator strength were calculated by the PCM-U-TDDFT method with the Gaussian09 program;⁴⁵ see Supporting Information page S5 and Table S2 for detail.

4. RESULTS AND DISCUSSION

4.1. Geometry and Localization/Delocalization Character. In the DFT-geometry optimization of **1** and **2**, we employed the M06 functional because the DFT method with the M06 functional provides the similar difference in energy between the C_1 - and C_2 -symmetrical geometries to the GMC-QDPT(SAS/SAS)-calculated one; see Supporting Information page S6 and Table S3.

In the Mn(III) complex **1**, we investigated the dependences of the characteristic geometrical parameters, the α -component

of dipole moment μ_x , and the difference in Helmholtz free energy between the C_1 - and C_2 -symmetrical geometries, $\Delta A(C_1-C_2)$, on the substituents (R^1, R^2) and the solvent species, as shown in Table 1; see Supporting Information page S7 for the computational procedure for dipole moment. In the case of **1c** bearing the asymmetrical salen ligand ($R^1 \neq R^2$), the large difference is observed between the M–O¹ and the M–O² distances, which indicates that **1c** exhibits the asymmetrical geometry even in gas phase; see Scheme 2 for the positions of O¹ and O² atoms. This asymmetrical geometry is consistent with the radical-localization and the large μ_x value of 12.8 D in gas phase. When going from gas phase to solution, μ_x becomes larger with the increase of the solvent polarity; 15.7 D in CH₂Cl₂ and 18.2 D in H₂O solution. This means that the solvation effect increases the extent of radical-localization, because the larger dipole moment induces larger stabilization of the solute in polar solvent.

In the case of the symmetrical salen ligand ($R^1 = R^2$), on the other hand, **1a** with (R^1, R^2) = (Me, Me) exhibits the asymmetrical geometry and the localized salen radical character even in gas phase, in which $\mu_x = 6.1 \text{ D}$. In contrast, **1b** with (R^1, R^2) = (OMe, OMe) has a structure similar to the C_2 -symmetrical one and the small dipole moment of $\mu_x = 0.5 \text{ D}$, which indicate the radical-delocalization. When going from gas phase to solution, these features of **1b** considerably change, as shown in Figure 1; it should be noted that μ_x increases to 9.1 D in **1a** and 10.5 D in **1b** even in weakly polar CH₂Cl₂ solution. Apparently, this radical-localization is caused by solvation effect. The asymmetrical geometry becomes more stable than the C_2 -symmetrical one by about 1.0 kcal mol^{–1} in free energy. In strongly polar H₂O solution, the stabilization of the asymmetrical geometry further increases to 2.5 kcal mol^{–1} relative to the C_2 -symmetrical one.

The 3D-RISM-SCF-U-DFT/M06 calculation indicates that the geometrical distortion and the localization/delocalization character of the Ni(II) complex **2** are similar to those of **1** in the asymmetrical ligand ($R^1 \neq R^2$) case but different in the symmetrical ligand ($R^1 = R^2$) case; see Table 2 for the characteristic geometrical parameters, the α -component of the dipole moment μ_x , and $\Delta A(C_1-C_2)$ in **2**. Actually, in CH₂Cl₂ solution, the geometries and the radical-delocalization characters of **2a** and **2b** differ little from those in gas phase, and hence, the geometry of the salen ligand is symmetrical, unlike **1a** and **1b**; see that the C¹–O¹ and the Ni–O¹ distances are almost the

(a) Complexes 1b and 2b in gas phase.

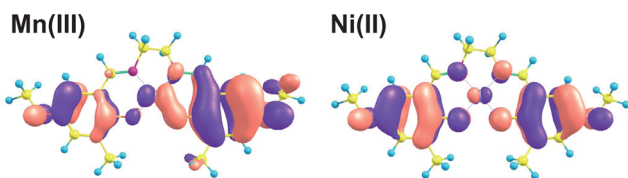
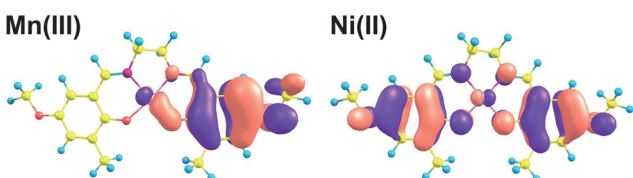
(b) Complexes 1b and 2b in CH₂Cl₂ solution.

Figure 1. α -Spin SOMO of one-electron oxidized Mn(III)– and Ni(II)–salen complexes with substituents (R^1, R^2) = (OMe, OMe) on the salen ligand.

same as the C^2-O^2 and the $Ni-O^2$ ones, respectively, in CH_2Cl_2 solution (Table 2). Also, μ_x is negligibly small unlike those of **1a** and **1b**. This means that **2a** and **2b** exhibit the larger radical-delocalization character than **1**. In strongly polar H_2O solution, however, **2a** and **2b** exhibit considerably large μ_x ; 9.3 D in **2a** and 11.9 D in **2b**. Consistent with this large μ_x , the C^1-O^1 and the $Ni-O^1$ distances are considerably different from the C^2-O^2 and the $Ni-O^2$ ones, respectively, in H_2O solution. These results indicate that the geometry and the localization/delocalization character of **2a** and **2b** are largely influenced by the polarity of solvent. Hence, the solvation effect is indispensable to correctly elucidate the mixed-valence character of these systems.

4.2. Difference in Bonding Interaction between Mn(III)– and Ni(II)–Salen Complexes. Three factors are considered as the possible reason for the difference in metal–salen interaction between the Mn(III) complex **1** and the Ni(II) analogue **2**: (i) One is the difference in formal charge of the metal center between the Mn(III) and the Ni(II), because the ES interaction between the metal center and the salen ligand depends on the charge of the metal center. (ii) The second is the difference in the number of d-electrons between these two metal species. Finally, (iii) the last is the difference in d orbital energy between the Mn(III) and the Ni(II).

To examine the charge effect of the metal center, the one-electron oxidized Cu(III)–salen analogue **3** with the substituents (R^1, R^2) = (Me, Me) was investigated as a model system, because **3** has the same d^8 electron configuration as that of the Ni(II) complex **2** but has +3 formal charge of the metal center like the Mn(III) complex **1**. The PCM-U-DFT/M06 calculation reveals that the ground state of **3** is not the same as that of **2**; the SCF calculation converged to the same ground state only when the exchange between occupied and unoccupied orbitals were restricted under the C_2 symmetry.⁴⁶ Hence, we performed the geometry optimization with the above-mentioned restriction and then calculated analytically the Hessian matrix; see Supporting Information page S8 for the ground state electronic structure of **3**. The Hessian matrix does not exhibit a negative eigenvalue, suggesting that **3** does not change from the C_2 -symmetrical structure to the asymmetrical one such as the Ni(II) complex **2** when **3** has the electronic state similar to the ground state of **2**. This result indicates that the difference in localization/delocalization character between **1** and **2** does not arise from the difference in the formal charge of the metal center.

In the localized salen radical, the π MO (HOMO) of the phenolate anion becomes the SOMO. Because the doubly occupied d_{π} orbital induces larger CT to the SOMO than the singly occupied d_{π} , the CT from the metal to the SOMO is larger in the Ni(II) complex **2** than in the Mn(III) complex **1**. Remember that the d_{xz} orbital is singly occupied in the Mn(III) but doubly occupied in the Ni(II); see Supporting Information page S9 and Table S4 for the evidence. If the electron population on the SOMO increases, the geometry of the phenoxyl radical deviates less from that of phenolate and vice versa. Hence the geometry difference between the phenolate and the phenoxyl radical is larger in the Mn(III) complex **1** than in the Ni(II) analogue **2**. This is because the CT occurs from the Ni d_{π} to the SOMO but the reverse CT occurs from the SOMO to the Mn d_{π} ; see also Tables 1 and 2. From these results, it is concluded that the presence of the doubly occupied d_{π} orbital decreases the localization character; in other words, the number of d electrons is one of the important factors for the localization/delocalization character and the d electron number enough to provide the doubly occupied d_{π} orbital is favorable for the delocalized electronic structure. The relation

Table 2. Important Geometrical Parameters, x -Component of Dipole Moment μ_x , and Difference in Free Energy between C_1 - and C_2 -Symmetrical Geometries, $\Delta A(C_1 - C_2)$, in One-Electron Oxidized Ni(II)–Salen Complexes

Ni(II) (<i>R</i> ¹ , <i>R</i> ²)	gas or solv.	sym.	L or D ^b	bond length ^a [Å]					
				C–O ¹	C–O ²	M–O ¹	M–O ²	μ _x ^c	Δ <i>A</i> (C ₁ –C ₂) ^d
<i>R</i> ¹ = <i>R</i> ² case									
2a (Me,Me)	gas	C ₂ -like	D	1.28	1.28	1.83	1.83	0.0	−0.02
	CH ₂ Cl ₂	C ₂ -like	D	1.28	1.28	1.84	1.84	0.0	−0.05
	H ₂ O	C ₁	L	1.31	1.27	1.84	1.87	9.3	−0.30
2b (OMe,OMe)	gas	C ₂ -like	D	1.30	1.30	1.84	1.84	0.0	−0.04
	CH ₂ Cl ₂	C ₂ -like	D	1.28	1.28	1.84	1.84	0.0	−0.08
	H ₂ O	C ₁	L	1.28	1.28	1.84	1.84	11.9	−0.68
<i>R</i> ¹ ≠ <i>R</i> ² case									
2c (Cl,OMe)	gas	C ₁	L	1.29	1.27	1.82	1.85	9.0	
	CH ₂ Cl ₂	C ₁	L	1.30	1.27	1.82	1.87	14.2	
	H ₂ O	C ₁	L	1.30	1.27	1.83	1.87	17.1	

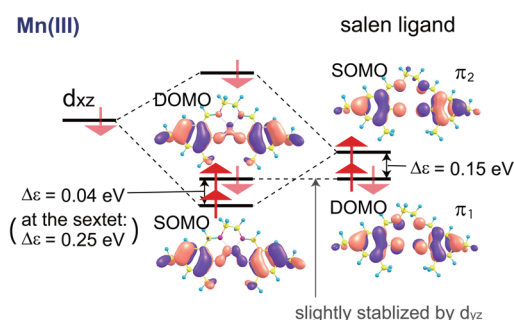
^aSee Scheme 2 for positions of O¹ and O² atoms. ^bL and D represent the localized and delocalized electronic states, respectively. ^cUnit is [Debye].

^dUnit is [kcal mol^{–1}]

between the d_{π} - π interaction and the d orbital energy will be discussed in the next subsection.

4.3. Effect of d Orbital Energy on the Difference between Mn(III) and Ni(II). The U-DFT/M06 and the 3D-RISM-SCF-U-DFT/M06 calculations indicate that the shape of the SOMO largely changes when going from the gas phase to the polar solution, as shown in Figure 1. This result suggests that the ease of the deformation of the SOMO is one of the important factors to determine the difference in the localization/delocalization character between the Mn(III) and Ni(II) complexes **1** and **2**. To make clear comparison between **1** and **2**, we examined the SOMO and its symmetry-counterpart DOMO at the C_2 -symmetrical geometry, where the SOMO consists of an antibonding combination of π MOs of two phenolate moieties and the symmetry-counterpart DOMO consists of a bonding combination; see Figure 2 for these MOs of **1a** and **2a** in gas phase.

(a) one-electron oxidized Mn(III)-salen complex, **1a**, with C_2 symmetry.



(b) one-electron oxidized Ni(II)-salen complex, **2a**, with C_2 symmetry.

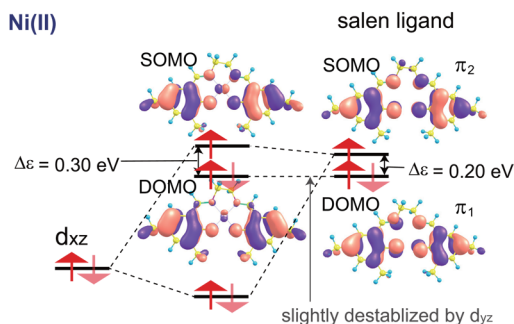


Figure 2. Energy diagram of d_{π} - π interacting orbitals of one-electron oxidized Mn(III)- and Ni(II)-salen complexes with substituents (R^1 , R^2) = (Me, Me) on the salen ligand. Values are calculated by energy of α -spin orbital calculated in gas phase.

Several important features are found in the energy diagram of the d_{π} - π orbitals at the C_2 -symmetrical geometry, as shown in Figure 2. (i) In the absence of the metal ion, the SOMO of the one-electron oxidized salen ligand exists at a higher energy than the DOMO by about 0.15–0.20 eV. (ii) In the Mn(III) complex **1**, the SOMO exists at a lower energy than the DOMO and the energy gap, $\Delta\epsilon$, decreases to 0.04 eV.⁴⁷ (iii) In the Ni(II) complex **2**, the SOMO exists at a higher energy than the DOMO and the $\Delta\epsilon$ value increases to 0.30 eV. These interesting differences between **1** and **2** are understood by considering the general trend that the d orbital energy becomes lower when going from the left- to the right-hand-side in the periodic table, as follows: Because the Mn d_{π} orbital exists at a higher energy than the SOMO, it lowers the SOMO energy and

hence the SOMO energy becomes lower than the DOMO. As a result, the orbital energy difference ($\Delta\epsilon$) between the SOMO and the DOMO becomes smaller because the SOMO exists at a higher energy than the DOMO before mixing. On the other hand, because the Ni d_{π} exists at a lower energy than the SOMO, it further raises the SOMO and hence the $\Delta\epsilon$ becomes larger. Hence, the orbital mixing between the SOMO and its symmetry-counterpart DOMO occurs easier in **1** than in **2**, leading to the larger radical-localization in **1** than in **2**.⁴⁸ Based on these results, it is concluded that the d orbital energy of metal element as well as the d electron number is one of the key factors to determine the localization/delocalization character of the metal–salen complexes.

4.4. Vertical Excitation Energy, Oscillator Strength, and Solvation Effect. Prior to the GMC-QDPT calculation, we performed the PCM-U-TDDFT calculations of the absorption spectrum in both of **1** and **2** but the vertical excitation energy $\Delta E_{\text{cond}}^{\text{avg}}$ and the oscillator strength $f_{\text{gr,ex}}^{\text{avg}}$ are very sensitive to the DFT functionals in comparison to the geometry optimization, suggesting that the high quality ab initio calculation based on the multireference theory is necessary for reliability; see Supporting Information page S5 and Table S2 for detail.

The vertical excitation energy $\Delta E_{\text{cond}}^{\text{avg}}$ and the oscillator strength $f_{\text{gr,ex}}^{\text{avg}}$ were evaluated in CH_2Cl_2 solution by using the 3D-RISM-SCF-DFT/M06-calculated solute geometry, \mathbf{R}^{opt} , and its equilibrium solvation structure, $g_{\text{gr}}(\mathbf{r})$. They are compared with the ΔE_{gas} and $f_{\text{gr,ex}}^{\text{gas}}$ values calculated in gas phase, as shown in Supporting Information Table S5. In gas phase, the GMC-QDPT(SAS/SAS)-calculated oscillator strength $f_{\text{gr,ex}}^{\text{gas}}$ indicates that **1b**, **2a**, and **2b** are classified into the class III mixed-valence compound but **1a** is classified into the class II mixed-valence compound like **1c** and **2c**; remember that the intensity of absorption spectrum of the class III mixed-valence compound is generally much larger than that of the class II compound. In CH_2Cl_2 solution, all $\Delta E_{\text{cond}}^{\text{avg}}$ values of **1** and **2** agree with the experimentally observed values. Though **1b** exhibits the absorption spectrum corresponding to delocalized electronic structure in gas phase, **1b** exhibits the class II mixed-valence character like **1a** in CH_2Cl_2 solution. The $\Delta E_{\text{cond}}^{\text{avg}}$ is calculated to be 1.11 eV for **1a**, 1.13 eV for **1b**, 0.49 eV for **2a**, and 0.45 eV for **2b**, which are close to the experimental values, 0.84, 0.98, 0.62, and 0.58 eV, respectively. This good agreement suggests that the solvation effect is indispensable to discuss the excitation energy and the localization/delocalization character of these mixed-valence compounds even in weakly polar CH_2Cl_2 solution; though these are the π - π absorption in the ligand, the Mn(III) and the Ni(II) centers play crucial roles in the absorption spectrum, as shown in Supporting Information page S10.

Though the experimentally observed tendency of absorption spectra is reproduced by the 3D-RISM-GMC-QDPT(SAS/SAS) calculation, the calculated vertical excitation energies ($\Delta E_{\text{cond}}^{\text{avg}}$) of the class II mixed-valence metal–salen complexes, **1a** and **1b**, are more or less overestimated like those of **1c** and **2c** in comparison to the experimental values, as shown in Supporting Information Table S5. Because the solvation effect is very important to reproduce well the excitation energy, we checked the reliability of the 3D-RISM-SCF method by making comparison with the MF-QM/MM-MD simulation,⁴⁹ where the geometry of the solute was taken from the 3D-RISM-SCF-U-DFT/M06-optimized one and the ensemble of solvent configurations was generated by the 1000 snapshots of the MF-

Table 3. Vertical Excitation Energy and Oscillator Strength Calculated at the GMC-QDPT(LAS/MAS) Level

		Mn(III)–salen complex			Ni(II)–salen complex		
gas or solv.	geom. ^a	1a (Me,Me)	1b (OMe,OMe)	1c (OMe,Cl)	2a (Me,Me)	2b (OMe,OMe)	2c (OMe,Cl)
Vertical Excitation Energy [eV]							
ΔE_{gas} in Gas Phase							
gas	gas ^a	0.869	0.441	1.459	0.656	0.653	0.820
gas	RISM ^a	0.963	0.932	1.424	0.650	0.638	0.899
$\Delta E_{\text{cond}}^{\text{avg}}$ in CH ₂ Cl ₂ Solution							
RISM	RISM	1.230	1.251	1.833	0.656	0.627	1.201
component ^b							
$\Delta E_{\text{solv}}^{\text{mf}}$	0.832	0.811	1.275	0.650	0.622	0.710	
$\Delta E_{\text{int}}^{\text{mf}}$	0.398	0.440	0.558	0.006	0.005	0.491	
expt. ^c	0.838	0.976	1.389	0.620	0.579	0.885	
Oscillator Strength [au]							
$f_{\text{gr,ex}}^{\text{gas}}$ in Gas Phase							
gas	gas	0.214	0.504	0.162	0.543	0.563	0.385
gas	RISM	0.197	0.239	0.160	0.539	0.551	0.326
$f_{\text{gr,ex}}^{\text{gas}}$ in CH ₂ Cl ₂ Solution							
RISM	RISM	0.170	0.194	0.149	0.539	0.535	0.270

^aOptimized in either gas phase or in CH₂Cl₂ solution at the U-DFT/M06 level. ^bComponent of $\Delta E_{\text{cond}}^{\text{avg}}$ at 3D-RISM-SCF-optimized geometry and solvent distribution. ^cReference 12.

QM/MM-MD trajectory with spacing of 3 ps. In the MF-QM/MM-MD simulation, the equation of motions of 1024 CH₂Cl₂ solvent molecules was solved under the periodic condition and the electronic structure of the solute was calculated at the MF-U-DFT/M06 level in the self-consistent manner; the parameters and the ES potential operator, $\hat{V}_{\text{int}}^{\text{p}}$, were taken to be the same as the 3D-RISM calculation. The MF-QM/MM-MD-calculated $\Delta E_{\text{cond}}^{\text{avg}}$ and $f_{\text{gr,ex}}^{\text{avg}}$ values are very close to the 3D-RISM-SCF-calculated values at the GMC-QDPT level; see Supporting Information Table S5. This result indicates that the 3D-RISM-SCF method provides the solvation structure similar to the MF-QM/MM-MD simulation and the 3D-RISM integral equation works well at least in the present systems. It is likely concluded that both methods can be successfully applied to the present systems; in other words, the solvation model is accurate and the difference between the experimental and the calculated vertical excitation energies arises from some other factor.

The 3D-RISM-GMC-QDPT(LAS/MAS) calculation provides the similar result to the 3D-RISM-GMC-QDPT(SAS/SAS)-calculated one, as shown in Table 3 and Supporting Information Table S5, indicating that the active space was reasonably taken here. **2a** and **2b** exhibit much larger oscillator strength, $f_{\text{gr,ex}}^{\text{avg}}$, than **1a** and **1b** by a factor of about three in both calculations. Though one may expect that the SAS to MAS active space extension more stabilizes the first excited state because of the explicit inclusion of the $d_{\pi} \rightarrow \pi$ excitation configurations, the active space extension unexpectedly leads to the increase of the $\Delta E_{\text{cond}}^{\text{avg}}$ value in the mixed-valence compounds except for **2c** in which the $\Delta E_{\text{cond}}^{\text{avg}}$ value moderately decreases.⁵¹ As a result, the 3D-RISM-GMC-QDPT(LAS/MAS)-calculated $\Delta E_{\text{cond}}^{\text{avg}}$ value becomes much closer to the experimental one than the 3D-RISM-GMC-QDPT(SAS/SAS)-calculated one in **2**. In particular, the $\Delta E_{\text{cond}}^{\text{avg}}$ values of the class III mixed-valence compounds **2a** and **2b** well agree with the experimental ones; the $\Delta E_{\text{cond}}^{\text{avg}}$ is calculated to be 0.66 (0.62) eV for **2a** and 0.63 (0.58) eV for **2b**, where in parentheses is an experimental value. This good agreement indicates that the SAS to MAS active space extension improves the description of the electronic interaction between two redox-active centers.

Though the agreement becomes better in the GMC-QDPT(LAS/MAS) calculation, the calculation with the SAS reproduces well the tendency experimentally reported. Also, the difference between GMC-QDPT(LAS/MAS) and GMC-QDPT(SAS/SAS) calculations is not large. In particular, the excitation energies and the CT characters of **1** and **2** differ little between the 3D-RISM-GMC-QDPT(SAS/SAS) and the 3D-RISM-GMC-QDPT(LAS/MAS) calculations except that the localized salen radical-character is moderately smaller in the MAS than in the SAS in both of the ground and the first excited states; see Supporting Information Tables S6 and S7. It is concluded that the GMC-QDPT(SAS/SAS)-calculated value is useful enough for discussing the localization/delocalization character of **1** and **2**.

4.5. CT Character of the Excitations of Mn(III)– and Ni(II)–Salen Complexes. To evaluate the CT character of excitations of **1** and **2**, we calculated the change of ESP charges on the solute moiety *i* at the 3D-RISM-GMC-QDPT level with eq 13:

$$\Delta Q_i = \sum_{\mu\nu} \Delta D_{\mu\nu}^{\text{PT}} \sum_{a \in \text{moiety } i} \langle \chi_{\mu} | \hat{Q}_a | \chi_{\nu}(\mathbf{R}) \rangle \quad (13)$$

Here, we separated the total system into such six moieties as metal atom *M*, substituents *R*¹ and *R*², two pairs of *o*-cyano-phenolate moieties which are hereafter denoted by (PhO+CN)¹ and (PhO+CN)², and the remaining moiety of the metal–salen complex, as shown in Scheme 3.

As shown in Table 4, the ESP charge on the (PhO+CN)¹ moiety increases by about 0.9 e but that on the (PhO+CN)² moiety decreases in a similar extent through the excitation,

Scheme 3. Separation of Total System into Six Moieties

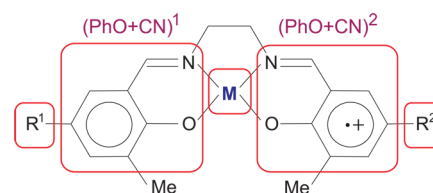


Table 4. Changes of ESP Charges by Vertical Excitation^a

moiety ^b	Mn(III)–salen complex			Ni(II)–salen complex		
	1a (Me,Me)	1b (OMe,OMe)	1c (OMe,Cl)	2a (Me,Me)	2b (OMe,OMe)	2c (OMe,Cl)
M	+0.01 ^c	+0.00	+0.01	+0.01	+0.01	+0.03
(PhO+CN) ¹	+0.88	+0.87	+0.88	−0.01	−0.01	+0.78
(PhO+CN) ²	−0.89	−0.87	−0.90	−0.01	−0.01	−0.81
R ¹	+0.00	+0.02	+0.03	+0.00	+0.00	+0.02
R ²	−0.00	−0.02	−0.02	+0.00	+0.00	−0.01
others	+0.00	+0.00	+0.00	+0.01	+0.02	−0.01

^aThe 3D-RISM-GMC-QDPT(LAS/MAS) method was employed. ^bSee Scheme 3 for position of each moiety. ^cUnit is electron [e].

indicating that the CT from the (PhO+CN)² to the (PhO+CN)¹ is significantly large, which corresponds to one-electron transfer from the (PhO+CN)² to the (PhO+CN)¹ moiety in both of **1a** and **1b** like **1c** and **2c**. In both of **2a** and **2b**, however, the ESP charges of the (PhO+CN)¹ and the (PhO+CN)² moieties change little by the excitation. Also, the ESP charges on the remaining four moieties change little by the excitations in **1** and **2**. These features of **1** and **2** differ little between the GMC-QDPT(LAS/MAS) and GMC-QDPT-(SAS/SAS) calculations; see Supporting Information Table S6. Based on these results, it is concluded that the (PhO+CN)¹ and the (PhO+CN)² moieties play crucial roles in inducing the solvation effect on the absorption spectrum, as will be discussed in section 4.6.

To clarify the electronic character of the first excited state, the total dipole moments of **1** and **2** were further analytically calculated in both of the ground and the first excited states at the 3D-RISM-GMC-QDPT level; see Supporting Information Table S7. In the class II mixed-valence compounds **1a** and **1b**, the *x*-component of the dipole moment μ_x considerably changes by the excitation, indicating that the vertical excitation exhibits the IVCT character. This is because the intramolecular electron transfer occurs from the electronically localized phenolate moiety to another electronically localized phenoxyl radical one; the sign of the very large μ_x becomes opposite when going from the ground state to the first excited one. In contrast, the μ_x value changes little by the excitation in **2a** and **2b**, indicating that the vertical excitation exhibits the CT character little between two electronically delocalized states; remember that the excitation occurs from one electronically delocalized state to another one in these complexes. These are characteristic features of the class II and III mixed-valence compounds. We wish to emphasize that the above results calculated at the 3D-RISM-GMC-QDPT level well agree with the experimental assignments reported by Kurahashi and Fujii.¹²

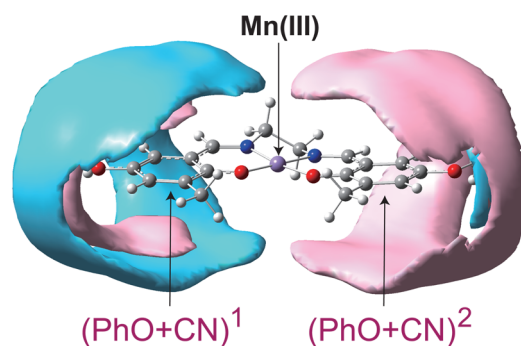
4.6. Reason Why Solvent Increases Excitation Energy in the Class II Mixed-Valence Complex but Does Not in the Class III Mixed-Valence Complex. Because the solvation effect is of considerable importance here, we wish to discuss the solvation effect in detail. To present microscopic insight into the solvation effect on the absorption spectrum, we examined the change in the spatial distribution function (SDF) of the solute–solvent ES interaction energy, $\Delta V_{\text{int}}^{\text{SDF}}(\mathbf{r})$, induced by the vertical excitation. The $\Delta V_{\text{int}}^{\text{SDF}}(\mathbf{r})$ is defined by eq 14,

$$\Delta V_{\text{int}}^{\text{SDF}}(\mathbf{r}) = \rho \sum_s q_s g_{\text{gr}}(\mathbf{r}) \cdot \{ \langle \bar{\Phi}_{\text{ex}}^{\text{mf}} | \hat{V}_{\text{int}}^{\text{P}}(\mathbf{R}, \mathbf{r}) | \bar{\Phi}_{\text{ex}}^{\text{mf}} \rangle - \langle \bar{\Phi}_{\text{gr}}^{\text{mf}} | \hat{V}_{\text{int}}^{\text{P}}(\mathbf{R}, \mathbf{r}) | \bar{\Phi}_{\text{gr}}^{\text{mf}} \rangle \} \quad (14)$$

The integration of the $\Delta V_{\text{int}}^{\text{SDF}}(\mathbf{r})$ over the entire 3D grid space of solvent, \mathbf{r} , corresponds to the $\Delta V_{\text{int}}^{\text{inf}}$ in eq 6.

To compare the solvation effect between the class II and III mixed-valence compounds, the 3D-RISM-GMC-QDPT(LAS/MAS)-calculated $\Delta V_{\text{int}}^{\text{SDF}}(\mathbf{r})$ of **1b** and **2b** is depicted in Figure 3, where the red region contributes to the increase of the $\Delta V_{\text{cond}}^{\text{avg}}$ and the blue region contributes to the decrease.

(a) one-electron oxidized Mn(III)-salen complex, **2a**.



(b) one-electron oxidized Ni(II)-salen complex, **2b**.

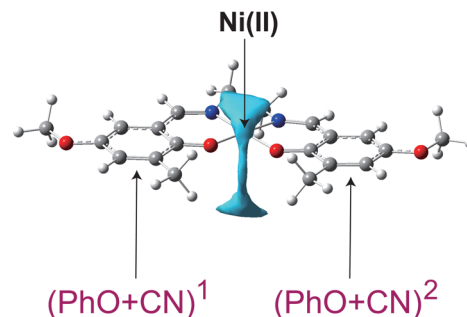


Figure 3. Change of solute–solvent ES interaction by excitation in one-electron oxidized Mn(III)– and Ni(II)–salen complexes with substituents (R^1 , R^2) = (OMe, OMe) on the salen ligand. Red region represents the increase in $\Delta E_{\text{cond}}^{\text{avg}}$ and blue region represents the decrease in it. (a) $|\Delta V_{\text{int}}^{\text{SDF}}(\mathbf{r})| = 0.1 \text{ kcal mol}^{-1} \text{ \AA}^{-3}$. (b) $|\Delta V_{\text{int}}^{\text{SDF}}(\mathbf{r})| = 0.01 \text{ kcal mol}^{-1} \text{ \AA}^{-3}$.

In **2b**, both the red and the blue regions are not observed near the solute, indicating that the solvation does not contribute to the change of the $\Delta V_{\text{cond}}^{\text{avg}}$. This is because the ESP charges on the solute moieties change little by the vertical excitation, as discussed in section 4.5. In contrast, the red and the blue regions are apparently observed near the (PhO+CN)¹ and the (PhO+CN)² moieties in **1b**. It is noted that the blue region near the (PhO+CN)¹ moiety is canceled out by the red region near the (PhO+CN)² moiety but the red region near the

(PhO+CN)¹ is not, leading to the conclusion that the red region near the (PhO+CN)¹ contributes to the increase of the $\Delta E_{\text{cond}}^{\text{avg}}$ in eq 4. From the analysis of the solvent distribution function, two important features were found, as follows: In one, the red region near the (PhO+CN)¹ corresponds to the distribution of the H site of CH₂Cl₂ solvent molecule. In other words, CH₂Cl₂ takes the H-interacting orientation in this red region, where the H site of CH₂Cl₂ is closer to the (PhO+CN)¹ moiety than the Cl one; remember that the water solvent takes the similar H-interacting orientation near the phenolate moiety.^{16b} Based on these results, it is concluded that the $\Delta E_{\text{cond}}^{\text{avg}}$ increases by solvation because the H-interacting solvation of CH₂Cl₂ stabilizes the (PhO+CN)¹ moiety by the ES attraction in the ground state but oppositely destabilizes it by the ES repulsion in the first excited state, as shown in Figure 4. This is because the CT occurs from the (PhO+CN)¹ to the

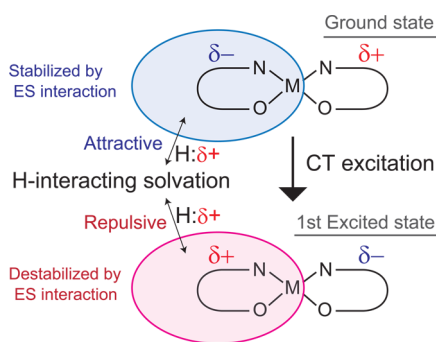
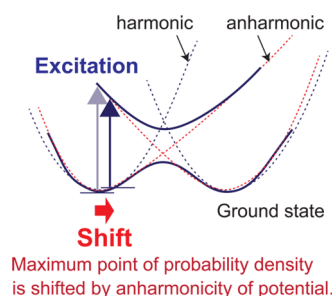


Figure 4. Schematic illustration of the increase in $\Delta E_{\text{cond}}^{\text{avg}}$ by solvation.

(PhO+CN)² by the excitation. Also, in both of **1b** and **2b**, the solvation around the remaining moieties of the metal–salen complexes are not important very much for the $\Delta E_{\text{cond}}^{\text{avg}}$.⁵⁰ Summarizing above discussion, it is concluded that the vertical excitation energy, $\Delta E_{\text{cond}}^{\text{avg}}$, of the class II compound increases by solvation because of the microscopic solvation, especially near the (PhO+CN)¹ moiety.

4.7. Other Factors to Be Considered in More Detail. In contrast to the delocalized absorption, the calculated $\Delta E_{\text{cond}}^{\text{avg}}$ value of the localized absorption is more or less larger than the experimental value. Even at the GMC-QDPT(LAS/MAS) level, the calculated $\Delta E_{\text{cond}}^{\text{avg}}$ values are overestimated in **1**; see Table 3. Three factors are considered as likely reasons for the overestimation: (i) The electronic relaxation energy of the solvent molecules is not taken into consideration in the present calculation; this relaxation energy is usually expected to decrease the $\Delta E_{\text{cond}}^{\text{avg}}$ because the deviation of the solvent electronic structure from the equilibrium one is larger in the excited state than in the ground state like that of the solvent configuration. (ii) The anharmonicity of the potential energy surface is not taken into consideration; the anharmonicity would decrease the excitation energy of the electronically localized state, because the vibrational mode on the anharmonic potential energy surface shifts the maximum probability position of the localized ground state toward the electronically delocalized state, as shown in Scheme 4. Remember that the delocalized state exists between two localized states that are separated with a low activation barrier. Also, (iii) the $\Delta E_{\text{cond}}^{\text{avg}}$ is evaluated by eq 4 in the present study, but this evaluation based on the MF approximation is not appropriate to represent the excitation energy, strictly speaking, when the transition dipole moment largely changes with the solvation coordinates, **V**. In

Scheme 4. Vibrational Contribution to the Vertical Excitation Energy



such a case, eq 15 is better than eq 4 to represent the excitation energy,

$$\Delta E_{\text{cond}}^{\text{avg}}(\mathbf{R}) \approx \frac{\int d\mathbf{V} \Delta E_{\text{cond}}^{\text{avg}}(\mathbf{R}, \mathbf{V}) P_{\text{gr}}(\mathbf{V}) I_{\text{gr,ex}}(\mathbf{V}; \mathbf{R})}{\int d\mathbf{V} P_{\text{gr}}(\mathbf{V}) I_{\text{gr,ex}}(\mathbf{V}; \mathbf{R})} \quad (15)$$

where $I_{\text{gr,ex}}(\mathbf{V}; \mathbf{R})$ is a transition probability function with respect to the solvation coordinate **V**, which directly depends on the absolute value of the transition dipole moment between the ground and the excited states.⁵² All these three points, (i–iii), contribute to the decrease of the $\Delta E_{\text{cond}}^{\text{avg}}$.

Some efforts have been made to include some of explicit solvation coordinates in the MF Hamiltonian. For instance, the theoretical model based on the RISM-SCF calculation has been proposed to solve the point (iii).^{53–56} However, its application to the present systems at the QMC-QDPT level is still difficult due to the huge computational demands as well as the points (i) and (ii). These three issues must be solved in a future work.

5. CONCLUSIONS

To investigate how much the electronic interaction is induced between two redox-active centers by the bridging metal species and why, we applied the three-regions 3D-RISM-SCF-U-DFT method to the optimization of both of the geometry and the solvation structure of the Mn(III) and Ni(II) complexes **1** and **2** and then calculated the vertical excitation energy, $\Delta E_{\text{cond}}^{\text{avg}}$, and the oscillator strength, $f_{\text{gr,ex}}^{\text{avg}}$, in the condensed phase at the GMC-QDPT level. The 3D-RISM-SCF-U-DFT/M06-calculated results indicate that **1** has the larger radical-localized electronic structure than **2**. The d electron numbers and the d orbital energy level are responsible for the difference in radical-localization/delocalization character between **1** and **2**, as follows: the unoccupied d_{π} orbital of the Mn(III) decreases the difference in orbital energy between the SOMO of the salen radical and its symmetry-counterpart DOMO at the C₂-symmetrical geometry but the doubly occupied d_{π} orbital of the Ni(II) increases it. This means that the orbital mixing occurs easier in **1** than in **2**, leading to the larger localization in **1** than in **2**.

The 3D-RISM-GMC-QDPT-calculated results suggest that the absorption spectrum of the Ni(II) complex **2** corresponds to the intramolecular electron excitation between two electronically delocalized states when the salen ligand is symmetrical but that of the Mn(III) complex **1** corresponds to the intramolecular electron transfer from the electronically localized state of one phenolate moiety to that of another phenoxyl radical one even when the salen is symmetrical. These results agree with the experimental assignments proposed by Kurahashi and Fujii.¹² Also, the 3D-RISM-GMC-QDPT

calculations clearly provide the microscopic solvation features, as follows: in the class III mixed-valence complex **2**, the electronic charge distribution changes little by the excitation, leading to little change in the $\Delta E_{\text{cond}}^{\text{avg}}$ by solvation. In the class II mixed-valence compound **1**, on the other hand, the H-interacting solvation of CH_2Cl_2 and H_2O near the electron-rich phenolate moiety stabilizes the ground state by the ES attraction but destabilizes the first excited state by the ES repulsion, because the CT of about 0.9 e occurs from the phenolate to the phenoxyl radical moiety by the excitation. Accordingly, the solvation effect increases the vertical excitation energy in the class II mixed-valence complex **1**.

The experimentally observed absorption energy was successfully reproduced by the 3D-RISM-GMC-QDPT method in the class III mixed-valence complex **2**. In particular, when all the five 3d orbitals are involved in the active space, the GMC-QDPT reproduces well the vertical excitation energy, $\Delta E_{\text{cond}}^{\text{avg}}$. In the class II mixed-valence complex **1**, the 3D-RISM-GMC-QDPT method reproduces well the experimentally observed tendency in the excitation energy and the radical-localization/delocalization character of **2**; though the calculated $\Delta E_{\text{cond}}^{\text{avg}}$ values are more or less overestimated, the energy difference is not large considering the complex electronic structure.

We wish to emphasize here that the microscopic solvation feature plays an important role in the radical-localization/delocalization character of these interesting Mn(III) and Ni(II) complexes and our 3D-RISM-GMC-QDPT method successfully discloses the importance in the microscopic solvation effect.

■ ASSOCIATED CONTENT

■ Supporting Information

Complete references of 44 and 45, details of difference in energy between quartet and sextet states of Mn(III)–salen complex, U-TDDFT-calculated results, effect of total charge of metal species, dependence of difference in energy between C_1 - and C_2 -symmetrical geometries on computational levels, dipole moments of Mn(III)– and Ni(II)–salen complexes, and selection of active space orbitals in GMC-QDPT calculation. This material is available free of charge via the Internet at <http://pubs.acs.org/>.

■ AUTHOR INFORMATION

Corresponding Author

*E-mail: sakaki.shigeyoshi.47e@st.kyoto-u.ac.jp.

Notes

The authors declare no competing financial interest.

■ ACKNOWLEDGMENTS

This work was financially supported by Grand-in-Aids for Specially Promoted Science and Technology (No. 22000009) and Grand Challenge Project (IMS, Okazaki, Japan) from the Ministry of Education, Culture, Sports, Science, and Technology. We are grateful to IMS computer for the supply of CPU time.

■ REFERENCES

- (1) Nelsen, S. F. *Chem.—Eur. J.* **2000**, *6*, 581–588.
- (2) Demadis, K. D.; Hartshorn, C. M.; Meyer, T. *Chem. Rev.* **2001**, *101*, 2655–2685.
- (3) Brunschwig, B. S.; Creutz, C.; Sutin, N. *Chem. Soc. Rev.* **2002**, *31*, 168–184.
- (4) Nishihara, H. *Bull. Chem. Soc. Jpn.* **2001**, *74*, 19–29.
- (5) Evangelio, E.; Ruiz-Molina, D. *Eur. J. Inorg. Chem.* **2005**, *15*, 2957–2971.
- (6) D'Alessandro, D. M.; Keene, F. R. *Chem. Soc. Rev.* **2006**, *35*, 424–440. D'Alessandro, D. M.; Keene, F. R. *Chem. Rev.* **2006**, *106*, 2270–2298.
- (7) Chisholm, M. H.; Patmore, N. J. *Acc. Chem. Res.* **2007**, *40*, 19–27.
- (8) Kaim, W.; Lahiri, G. K. *Angew. Chem., Int. Ed.* **2007**, *46*, 1778–1796.
- (9) Glover, S. D.; Goeltz, J. C.; Lear, B. J.; Kubiak, C. P. *Eur. J. Inorg. Chem.* **2009**, *5*, 585–594.
- (10) Creutz, C.; Taube, H. J. *J. Am. Chem. Soc.* **1969**, *91*, 3988–3989. Creutz, C.; Taube, H. J. *J. Am. Chem. Soc.* **1973**, *95*, 1086–1094.
- (11) Robin, M. B.; Day, P. *Adv. Inorg. Chem. Radiochem.* **1967**, *10*, 247–422.
- (12) Kurahashi, T.; Fujii, H. *J. Am. Chem. Soc.* **2011**, *133*, 8307–8316.
- (13) Kurahashi, T.; Kikuchi, A.; Tosha, T.; Shiro, Y.; Kitagawa, T.; Fujii, H. *Inorg. Chem.* **2008**, *47*, 1674–1686.
- (14) Storr, T.; Wasinger, E. C.; Pratt, R. C.; Stack, T. D. P. *Angew. Chem., Int. Ed.* **2007**, *46*, 5198–5201.
- (15) Shimazaki, Y.; Stack, T. D. P.; Storr, T. *Inorg. Chem.* **2009**, *48*, 8383–8392.
- (16) (a) Aono, S.; Sakaki, S. *J. Phys. Chem. B* **2012**, *116*, 13045–13062. (b) Aono, S.; Hosoya, T.; Sakaki, S. *Phys. Chem. Chem. Phys.* **2013**, *17*, 6368–6381.
- (17) Chandler, D.; Anderson, H. C. *J. Chem. Phys.* **1972**, *57*, 1930–1931.
- (18) Hirata, F.; Rossky, P. J. *Chem. Phys. Lett.* **1981**, *83*, 329–334.
- (19) Ten-no, S.; Hirata, F.; Kato, S. *Chem. Phys. Lett.* **1993**, *214*, 391–396. Ten-no, S.; Hirata, F.; Kato, S. *J. Chem. Phys.* **1994**, *100*, 7443–7453.
- (20) Sato, H.; Hirata, F.; Kato, S. *J. Chem. Phys.* **1996**, *105*, 1546–1551.
- (21) Chandler, D.; McCoy, J.; Singer, S. J. *Chem. Phys.* **1986**, *85*, 5971–5976. Chandler, D.; McCoy, J.; Singer, S. J. *Chem. Phys.* **1986**, *85*, 5977–5982.
- (22) Beglov, D.; Roux, B. J. *Chem. Phys.* **1995**, *103*, 360–364.
- (23) Beglov, D.; Roux, B. J. *Phys. Chem. B* **1997**, *101*, 7821–7826.
- (24) Du, Q.; Beglov, D.; Roux, B. J. *Phys. Chem. B* **2000**, *104*, 796–805.
- (25) Kovalenko, A.; Hirata, F. *J. Phys. Chem. B* **1999**, *103*, 7942–7957. Kovalenko, A.; Hirata, F. *J. Chem. Phys.* **1999**, *110*, 10095–10112.
- (26) Yoshida, N.; Hirata, F. *J. Comput. Chem.* **2006**, *27*, 453–462.
- (27) Ebisuzaki, R.; Watanabe, Y.; Nakano, H. *Chem. Phys. Lett.* **2007**, *442*, 164–169. Nakano, H.; Uchiyama, R.; Hirao, K. *J. Comput. Chem.* **2002**, *23*, 1166–1175.
- (28) Ray, K.; Petrenko, T.; Wiegardt, K.; Neese, F. *Dalton Trans.* **2007**, *16*, 1552–1566.
- (29) The LJ potential term of $\hat{V}_{\text{int}}^{\text{p}}(\mathbf{R}, \mathbf{r})$ is omitted in eq 8, because the LJ interaction is here represented by the classical parameters which are independent of the positions of the solute electrons.
- (30) Hilborn, R. C. *Am. J. Phys.* **1982**, *50*, 982–986.
- (31) Condon, E. U. *Phys. Rev.* **1928**, *32*, 858–872.
- (32) Yamazaki, S.; Kato, S. *Chem. Phys. Lett.* **2004**, *386*, 414–418.
- (33) Higashi, M.; Kato, S. *J. Phys. Chem.* **2005**, *109*, 9867–9874.
- (34) Mori, T.; Kato, S. *J. Chem. Phys.* **2010**, *133*, 064107.
- (35) (a) From the viewpoint of the oxidation catalyst, the chirality of the metal–salcn complex plays an important role in the synthesis of other chiral products.^{35b} However, it is of no importance in the understanding of the localized and the delocalized characters of the metal–salcn complexes; see section 4.5. (b) McGarrigle, E. M.; Gilheany, D. G. *Chem. Rev.* **2005**, *105*, 1563–1602.
- (36) Zhao, Y.; Truhlar, D. G. *Theor. Chem. Acc.* **2008**, *120*, 215–241.
- (37) In both of the Mn(III) and Ni(II) complexes **1** and **2**, we failed to include an unoccupied 3d_{xy} orbital in the small active space (SAS) because it exists at a considerably high energy. In **2**, we failed to include four doubly occupied 3d orbitals in the SAS, because they are at much lower energy than the metal–ligand σ orbitals. To include

these d orbitals, the very large active space (LAS) is needed; see Supporting Information pages S3 and S4.

(38) In GMCSCF calculations, the LASs (31e, 30o) and (35e, 34o) were employed for the Mn and Ni complexes **1** and **2**, respectively. Then, we selected 25 orbitals for the medium active space (MAS) by removing five orbitals (ψ_{01} , ψ_{02} , ψ_{03} , ψ_{15} , and ψ_{16} in Figure S4a) and nine orbitals (ψ_{01} , ψ_{02} , ψ_{03} , ψ_{10} , ψ_{11} , ψ_{12} , ψ_{13} , ψ_{15} , and ψ_{16} in Supporting Information Figure S4b) from the LASs of **1** and **2**, respectively, to reconstruct the reference states and performed the successive QDPT calculation; see Supporting Information pages S3 and S4 and Figure S4. Even when these orbitals were removed, all the five 3d orbitals were involve in the active space. Employing this procedure, we could reduce computational costs in calculating the vertical excitation energy and the oscillator strength. Note that the $d_\pi \rightarrow \pi$ excitations are already involved in the SAS of the Mn(III) complex **1** because the singly occupied d_π can be easily involved in the active space of **1**.

(39) Dolg, M.; Wedig, U.; Stoll, H.; Preuss, H. *J. Chem. Phys.* **1987**, *86*, 866–872.

(40) Dunning, T. H., Jr. *J. Chem. Phys.* **1989**, *90*, 1007–1023. Woon, D. E.; Dunning, T. H., Jr. *J. Chem. Phys.* **1993**, *98*, 1358–1371.

(41) Fox, T.; Kollman, P. A. *J. Phys. Chem. B* **1998**, *102*, 8070–8079.

(42) Berendsen, H. J. C.; Postma, J. P. M.; van Gunsteren, W. F.; Hermans, J. In *Intermolecular Forces*; Pullman, B., Ed.; Reidel: Dordrecht, 1981; pp 331–342.

(43) Cornell, W. D.; Cieplak, P.; Bayly, C. I.; Gould, I. R.; Merz, K. M., Jr.; Ferguson, D. M.; Spellmeyer, D. C.; Fox, T.; Caldwell, J. W.; Kollman, P. A. *J. Am. Chem. Soc.* **1995**, *117*, 5179.

(44) Schmidt, M. W.; Baldridge, K. K.; Boatz, J. A.; et al. *J. Comput. Chem.* **1993**, *14*, 1347–1363 See Supporting Information page S2 for the complete reference.

(45) Frisch, M. J. et al. *GAUSSIAN 09*, Revision B.01, Gaussian, Inc.: Wallingford, CT, 2010. See the Supporting Information page S2 for the complete reference.

(46) The SCF calculation was performed by starting from the $(\pi_1)^2(\pi_2)^1$ electron configuration and the optimized MOs of the Ni(II) complex **2**.

(47) In Figure 2a, the SOMO (π_2) exists at a lower energy than the DOMO (π_1) in the ground state electron configuration of the Mn complex **1**. This is seemingly unreasonable but this is correct because important is not the orbital energy but the energy of electronic state. When the SCF calculation was started from the $(\pi_1)^1(\pi_2)^2$ electron configuration and the exchange between the occupied and unoccupied orbitals was restricted, the U-DFT/M06 calculation provided the higher α -spin orbital energy of the singly occupied π_1 than that of the doubly occupied π_2 but the total energy of the $(\pi_1)^1(\pi_2)^2$ electron configuration became unstable by 5.6 kcal mol⁻¹. Another reasonable explanation is found in the π_1 and π_2 orbital energies of the nonoxidized Mn(III)–salen complex. We calculated them and found that the π_2 β -spin orbital energy exists at a higher energy than the π_1 β -spin orbital by 0.30 eV and hence the β -spin ionization occurs from the π_2 upon the one-electron oxidization of the Mn(III)–salen complex. In Figure 2, we displayed the α -spin orbital energies because we want to discuss the orbital energy difference between the π_1 and π_2 orbitals; remember that the comparison between the occupied π_1 and the unoccupied π_2 in the β -orbital is not reasonable.

(48) The sextet state of the Mn(III) complex **1** exhibits the larger $\Delta\epsilon$ than the quartet state by about 0.2 eV; this feature is also consistent with the U-DFT- and the 3D-RISM-SCF-U-DFT-calculated results that the localization of the salen radical occurs easier in the quartet state than in the sextet state.

(49) Yamamoto, T. *J. Chem. Phys.* **2008**, *129*, 244104. Nakano, H.; Yamamoto, T. *J. Chem. Theory Comput.* **2012**, *9*, 188–203.

(50) This result also justifies that the model system can be reasonably employed for the investigation of the absorption spectra in solution, as shown in Supporting Information Figure S1.

(51) The reason is still unclear in the present study.

(52) In the one-electron oxidized Mn(III) and Ni(II)–salen complexes, the transition probability function, $I_{\text{gr,ex}}(\mathbf{V};\mathbf{R})$, increases

when going from the localized electronic structure to the delocalized one.

(53) Naka, K.; Morita, A.; Kato, S. *J. Chem. Phys.* **1999**, *110*, 3484–3492.

(54) Yamazaki, S.; Kato, S. *J. Chem. Phys.* **2005**, *123*, 114510.

(55) Mori, T.; Kato, S. *J. Chem. Phys.* **2010**, *133*, 064107.

(56) Aono, S.; Minezawa, N.; Kato, S. *Chem. Phys. Lett.* **2010**, *492*, 193–197. Aono, S.; Yamamoto, T.; Kato, S. *J. Chem. Phys.* **2011**, *134*, 144108.